Bimetallic Ni-Hf tellurides as an advanced electrocatalyst for overall water splitting with layered g-C$_3$N$_4$ modification

Tong Li [a], Jiang Wu [a, *], Lingxia Qiao [a], Qunzhi Zhu [a], Zaiguo Fu [a], Jia Lin [b], Jing Chen [b], Lin Peng [b], Baofeng Wang [c], Zhongwei Chen [d, **]

[a] College of Energy and Mechanical Engineering, Shanghai University of Electric Power, Shanghai 200090, China
[b] College of Mathematics and Physics, Shanghai University of Electric Power, Shanghai 200090, China
[c] College of Environmental and Chemical Engineering, Shanghai University of Electric Power, Shanghai 200090, China
[d] Department of Chemical Engineering, Waterloo Institute for Nanotechnology, University of Waterloo, Canada Ontario, Canada

ARTICLE INFO

ABSTRACT

Impressive developments have been achieved in the field of bifunctional electrocatalysts for the overall water splitting in alkaline and weak alkaline electrolytes but still challenging. Herein, we have coupled the early and later transition metals to form novel bimetallic tellurides electrocatalyst for overall water splitting by simple one-step hydrothermal. Because of the large specific surface area of g-C$_3$N$_4$ as substrates, the as-prepared NiTe-HfTe$_2$/g-C$_3$N$_4$ displays appealing electrocatalytic activity and satisfactory stability in both oxygen evolution reaction and hydrogen evolution reaction in alkaline media. Furthermore, the electrolytic cell with two electrodes assembled by NiTe-HfTe$_2$/g-C$_3$N$_4$ demonstrates the same excellent performance in overall water splitting. The strong electronegativity of Te and the synergistic effect between Ni and Hf together contribute to the overall water splitting process. This work provides a novel strategy for the design of bifunctional transition metal−based electrocatalyst to achieve efficient and stable overall water splitting.

© 2022 Elsevier Ltd. All rights reserved.

1. Introduction

Recently, global environmental issues have received increasing attentions due to the excessive global consumption of fossil fuels and massive anthropogenic emissions of greenhouse gas. Renewable energy is an effective strategy for solving global energy problem, and therefore, researchers are focusing much effort on developing secure, green, sustainable new technologies for future energy sources [1−5]. Among lots of renewable energy sources, hydrogen is regarded as the most competitive candidate for next-generation clean fuel because of satisfactory energy density with zero carbon emission and pure water recycling [6−8]. Hence, many endeavors have been devoted to improve the efficiency of hydrogen production in recent years. Among the many strategies to produce hydrogen, electrochemical water splitting has great industrial potential and is a convenient, sustainable, and non-polluting production path, making it a research hotspot. However, the overall water splitting, consisting of hydrogen evolution reaction (HER) at cathode and oxygen evolution reaction (OER) at anode, is hindered by the sluggish kinetics with large overpotential at two electrodes [9−12]. The most important task for water splitting is the discovery of high-effective electrocatalysts, which can lower energy barrier and improve the energy efficiency. Despite Pt-based and Ru-based electrocatalysts being considered as most efficient HER and OER catalysts reported, the unacceptable cost and the scarcity of such precious-metal-based electrocatalysts deeply restrict their large-scale industrial water splitting applications widely [13−16]. Therefore, enormous efforts have been invested in finding alternatives to precious metal electrocatalysts for HER and OER, being composed of non-precious metals and non-metallic elements, which are effective in improving both catalytic activity and stability.

In past decade years, numerous non-noble-metal-based water splitting electrocatalysts, especially transition metal−based materials oxides [17,18], nitrides [19,20], phosphides [21,22] and chalcogenides [23,24], have been extensively researched. Among these advanced materials, later transition metal (e.g. Fe [25,26],

Co [27,28] and Ni [29,30]) chalcogenides (e.g., O [31,32], S [33,34], Se [35,36], and Te [37,38])-based electrocatalysts have been widely reported because of their earth abundance, outstanding electrical conductivity and excellent catalytic activity. Meanwhile, early transition metals (e.g. Ti, Zr, and Hf) also exhibit unexpected electron conductivity and promising catalytic potential [39]. Ti, Zr, and Hf are located in group 3, which are the early transition metal elements, whereas Fe, Co, and Ni are later transition metal elements, which are located in groups 8, 9, and 10, respectively. Based on the previous literature reported [40,41], water splitting activity is deeply related to the number of d-electrons in the transition metal ions of perovskite oxides, that is, the early transition metal oxides represent lower activity and the later transition metal oxides own higher activity. However, the relationship between the reactivity of transition metal chalcogenides and valence electrons is currently unclear, and more accurate models are required to explore the reactivity trend. It is reported that the synergistic effect of early and later transition metal elements could effectively lower the reaction energy barrier of important intermediates, (OH*, O*, OOH*), greatly improving the efficiency of overall water splitting. Therefore, we have studied the electrochemical properties of the bimetallic tellurides in the field of overall water splitting, which is combined with early transition and later transition metals.

Based on the previously mentioned considerations, an advanced heterogeneous nanomaterial was successfully coupled by simple one-step solvothermal method, consisting of NiTe and HfTe$_2$. Because of the strong synergy between the early and later transition metals, NiTe-HfTe$_2$ was anchored onto the ultrathin layered g-C$_3$N$_4$, which possesses a large specific surface area as a substrate, promoting the exposure of abundant active sites. As envisaged, the prepared NiTe-HfTe$_2$/g-C$_3$N$_4$ electrocatalysts possess excellent bifunctional electrocatalytic performance and exhibit satisfactory OER and HER electrocatalytic activity in both alkaline and weak alkaline electrolytes. In fact, in the standard three-electrode system we have prepared, only ultra-low overpotentials of 150, 220, and 260 mV are required for NiTe-HfTe$_2$/g-C$_3$N$_4$ electrode to drive up to current densities of 10, 50, and even 100 mA/cm^2 in OER process, respectively. The as-prepared NiTe-HfTe$_2$/g-C$_3$N$_4$ electrocatalysts exhibit outstanding HER electrocatalytic activity as well, ultra-low overpotentials of 71, 250, and 340 mV are needed for H$_2$ evolution to reach to current densities of 10, 50, and 100 mA/cm^2 in regular alkaline electrolytes (0.1 M KOH), respectively. Furthermore, the experimental electrolyzer assembled by as-prepared NiTe-HfTe$_2$/g-C$_3$N$_4$ electrodes requires only ultra-low voltage of 1.49, 1.6, and 1.69 V to induce full water splitting current densities of 10, 50, and 100 mA/cm^2, which is superior to that of precious-metal-based electrodes. As expected, advanced bimetallic tellurides−based electrocatalysts also possess excellent electrochemical stability during ultra-long time (100 h) overall water splitting, remaining close to 100% current densities of initial values at different working voltages in 0.1 M KOH solution.

2. Experimental section

2.1. Chemicals and reagents

Hafnium (IV) chloride (HfCl$_4$, 99.9%), Nickel (II) nitrate hexahydrate (Ni(NO$_3$)$_2$·6H$_2$O, 99%), tellurium (Te, 99.99%), sodium borohydride (NaBH$_4$, 98%), melamine (C$_3$H$_6$N$_6$, 99%), ethanol (C$_2$H$_5$OH, 99.7%), deionized water (H$_2$O), nafion (5 wt%), ruthenium (IV) oxide (RuO$_2$, 99.95%), and platinum on carbon (Pt/C, 20 wt%) were all purchased from Shanghai Titan Scientific Co., Ltd. All chemical reagents were used without further purification.

2.2. Preparation of ultrathin layered g-C$_3$N$_4$

In the classical synthesis, 10 g of melamine was placed in a crucible with a lid and heated from room temperature to 550°C at a heating rate of 2.5°C min^{-1}, holding for 4 h. The resulting yellow blocks, bulk g-C$_3$N$_4$, were ground to yellow powders. Three grams of the yellow powders were placed in an open porcelain boat without a lid and heated from room temperature at a heating rate of 2.5°C min^{-1} to 520°C, holding for another 2.5 h. The near-white product obtained after ground was the ultrathin layered g-C$_3$N$_4$.

2.3. Preparation of NiTe-HfTe$_2$/g-C$_3$N$_4$

Generally, Ni foams (0.5 cm × 0.5 cm) were sonicated in acetone for 30 min to remove the oxides from the surface, then sonicated in ethanol and deionized water for 10 min. Treated Ni foams were dried in vacuum drying oven at 60°C for 6 h. In the classical synthesis, 1.16 g of Ni(NO$_3$)$_2$·6H$_2$O, 1.28 g of HfCl$_4$, and 40 mg of g-C$_3$N$_4$ were added into 30 mL of ethanol for 2 h magnetic stirring to form the light green homogeneous solution. At the same time, 0.51 g of Te powders and 0.04 g of NaBH$_4$ were put into 40 mL of ethanol for 2 h magnetic stirring to form the gray homogeneous solution. Then, the green and gray homogeneous solutions were mixed together and kept stirring for another 2 h. The stirred solution was placed into a 100 mL Teflon-lined stainless autoclave and kept at a temperature of 180°C for 6 h. After natural cooling, the resulting product was collected by centrifugation and washed three times with ethanol and deionized water, respectively, and stored in a vacuum drying oven for 12 h. Finally, the product was ground to obtain NiTe-HfTe$_2$/g-C$_3$N$_4$. For comparison, the NiTe-HfTe$_2$ was synthesized at the same reaction conditions except without the addition of g-C$_3$N$_4$. The NiTe was synthesized at the same reaction conditions except without the addition of g-C$_3$N$_4$ and HfCl$_4$.

2.4. Characterization

The as-prepared samples were used the X-ray diffraction (XRD; Rigaku Ultima IV) patterns to examine the phase compositions at the 2θ range of 5−90° (5° min^{-1}) with a Cu Kα X-ray source (λ = 1.5418 Å). X-ray photoelectron spectroscopy (XPS) spectra were collected on an X-ray photoelectron spectrometer of Thermo Scientific K-Alpha, equipped with an X-ray source (Al Kα) at hν = 1,486.6 eV. The microstructure was observed by field emission scanning electron microscope (Sigma 300), transmission electron microscopy (FEI Teg-C3N4ai F30), and high-resolution transmission electron microscopy (HRTEM; TECNAL G2 TF20). Energy-dispersive X-ray (EDX, Smart EDX) were obtained to probe the chemical composition of the materials. N$_2$ adsorption/desorption isotherms (ASAP 2460 2.01, −195.8°C) was obtained to study the surface area of the samples.

2.5. Electrochemical measurement

Two milligrams of NiTe-HfTe$_2$/g-C$_3$N$_4$ powders were dispersed in 1 mL solvent containing 195 μL of isopropyl alcohol, 780 μL of deionized water, and 25 μL of 5 wt% Nafion to form a homogeneous ink by sonication for 30 min. The ink density loaded in Ni foam is ~0.2 mg/cm^2. The electrochemical tests for OER and HER performance were carried out in a standard three-electrode system controlled by a CHI760D electrochemical workstation. An Hg/HgO electrode with a 1.0 M KOH solution and a carbon rod were used as reference and counter electrodes, respectively. The polarization curves were recorded by linear sweep voltammetry with a scan rate of 5.0 mV/s. All the initial data were calibrated with 85% iR

compensation, and the potentials were transferred to a reversible hydrogen electrode (RHE) using the following formula.

$$E_{vs.RHE} = E_{vs.Hg/HgO} + 0.098V + 0.059 \times PH \tag{1}$$

where $E_{vs.RHE}$ is the converted potential versus RHE, $E_{vs.Hg/HgO}$ is the experimental potential measured against Hg/HgO, and 0.098 V is the standard potential of Hg/HgO at 25°C.

Electrochemical impedance spectroscopy (EIS) was operated on the same three electrodes in a 0.1 M KOH electrolyte with a frequency range of $0.01-10^5$ Hz, and the amplitude was 5 mV.

3. Results and discussion

### 3.1. Surface morphology and structure analysis

NiTe-HfTe$_2$/g-C$_3$N$_4$ electrocatalyst has been exploited as a promising alternative to precious-metal-based catalysts for overall water splitting with a wide range of applications by a versatile and easy synthetic route, as illustrated in Scheme 1. We prepared ultrathin layered g-C$_3$N$_4$ with a large specific surface area by a two-step thermal peeling method (Fig. S7c). From the SEM image of NiTe (Fig. S7b), it could be clearly observed that many regular nanosheets seem to coalesce into flower-like nanostructures. Interestingly, the SEM images of NiTe-HfTe$_2$ (Fig. S7a) show that the NiTe nanosheets are clustered into larger irregular clusters, which is perhaps due to the addition of Hf elements making the NiTe growth irregular, facilitating the stabilization of the rivet on the g-C$_3$N$_4$. Unsurprisingly, the NiTe-HfTe$_2$ clusters were uniformly grown in situ on the ultrathin layered g-C$_3$N$_4$ surface to coupling the NiTe-HfTe$_2$/g-C$_3$N$_4$ sample by one-step solvothermal method (Fig. 1a and b). The HRTEM image of NiTe-HfTe$_2$/g-C$_3$N$_4$ (Fig. 2a) displays lattice fringe of 0.29 and 0.23 nm, corresponding to the (101) crystal plane of NiTe and the (102) crystal plane of HfTe$_2$, the SAED spectrum (Fig. S9a) identifies polycrystalline diffraction rings corresponding to the (202) facet of NiTe and the (223) facet of HfTe$_2$, which further corroborates the successful synthesis of NiTe and HfTe$_2$. In addition, EDX spectrum for NiTe-HfTe$_2$/g-C$_3$N$_4$ (Fig. S14) reveals Ni, Hf, Te, C, and N peaks, confirming the existence of NiTe and HfTe$_2$. Furthermore, the EDX elemental mapping images of NiTe-HfTe$_2$/g-C$_3$N$_4$ demonstrate that Ni, Hf, Te, C, and N elements (Fig. 2c−g) are evenly distributed in the as-prepared samples, meaning the successful coupling of NiTe-HfTe$_2$/g-C$_3$N$_4$. We also used N$_2$ adsorption−desorption isotherm to detect the effect of the addition of ultrathin layered g-C$_3$N$_4$ on the specific surface areas (Fig. 2h). In fact, although pure g-C$_3$N$_4$ has the largest BET surface areas (170.6 m^2/g), the BET-specific surface area of NiTe-HfTe$_2$/g-C$_3$N$_4$ (126.2 m^2/g) with the addition of g-C$_3$N$_4$ is greatly increased compared with bare NiTe-HfTe$_2$ (86.8 m^2/g) and NiTe (27.3 m^2/g). The pore sizes of four as-prepared samples behave the same trend, which were calculated by Barrett-Joyner-Halenda method as 13.4 (NiTe-HfTe$_2$/g-C$_3$N$_4$), 3.5 (NiTe-HfTe$_2$), 3.3 (NiTe), and 20.8 (g-C$_3$N$_4$) nm, respectively (Fig. 2i). Nevertheless, the surface functional groups and chemical bonds of NiTe-HfTe$_2$/g-C$_3$N$_4$ are still unknown, and additional chemical characterization is necessary.

3.2. Crystal and chemical composition analysis

To identify the chemical composition and the crystalline phases of NiTe-HfTe$_2$/g-C$_3$N$_4$, NiTe-HfTe$_2$, NiTe, and g-C$_3$N$_4$, XRD pattern analysis was applied to characterize the basic properties of four as-prepared samples. As displayed in Fig. 3a, the XRD pattern of NiTe displays diffraction signals located at 31.7°, 42.4°, 53.8°, 56.1°, 70.1°, 71.8°, and 76.4°, matching well with the characteristic (101), (102), (200), (201), (004), (210), and (203) crystal planes of the pure NiTe phase (JCPDS No. 89–2018). NiTe-HfTe$_2$ and NiTe-HfTe$_2$/g-C$_3$N$_4$ possess the same characteristic peaks as NiTe, as well as characteristic signals at 27.2°, 47.5°, 55.4°, 61°, and 86.1°, which are corresponding to the characteristic (100), (110), (201), (112), and (300) crystal planes of the homogeneous HfTe$_2$ phase (JCPDS No. 26–0736), demonstrating the successful coupling of NiTe and HfTe$_2$. Interestingly, no diffraction peaks attributed to g-C$_3$N$_4$ are obviously observed in the XRD image of NiTe-HfTe$_2$/g-C$_3$N$_4$, which could be attributed to the fact that the g-C$_3$N$_4$ content in the as-prepared sample is too low to satisfy the detection requirements of the instrument and thus could not be detected.

The chemical state and chemical compositions of Ni, N, Hf, and Te elements in the as-prepared NiTe-HfTe$_2$/g-C$_3$N$_4$ could be proved
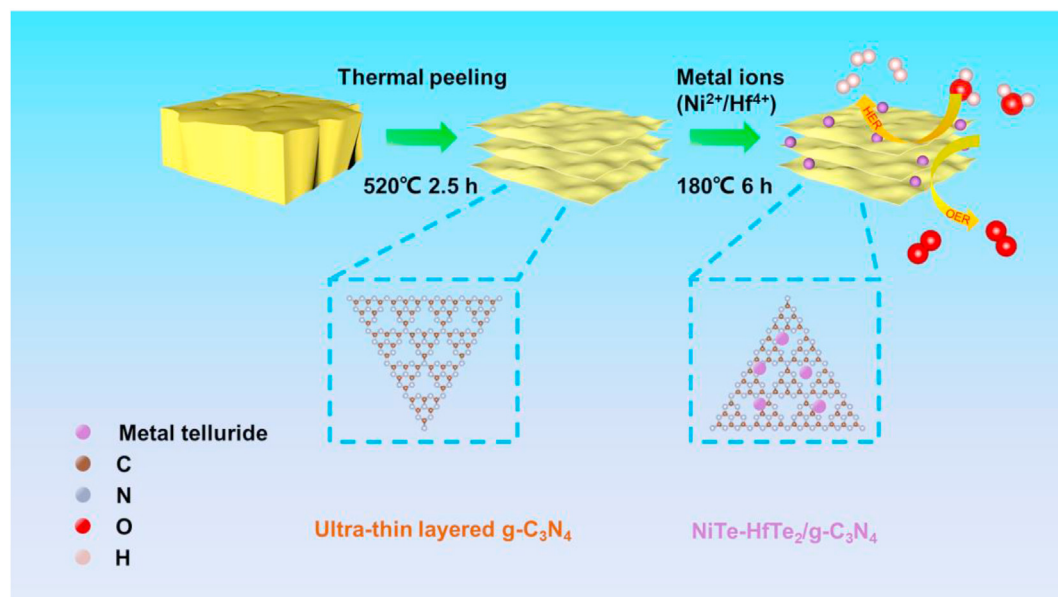
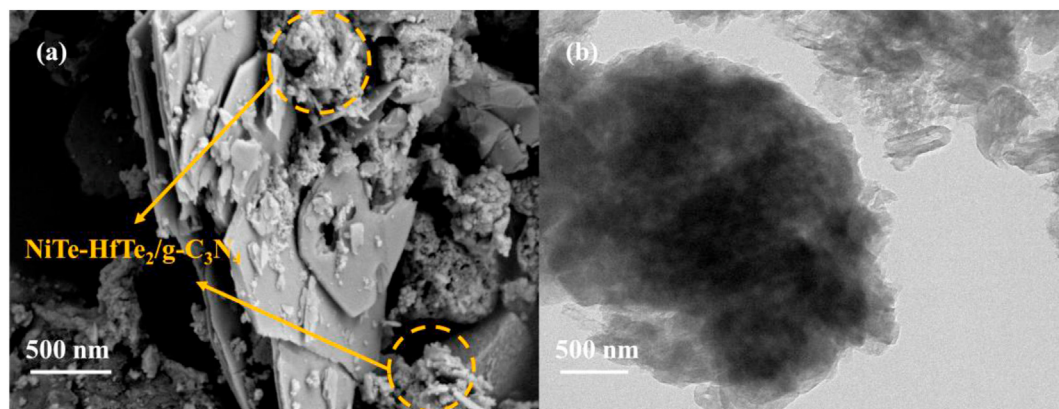**Scheme 1.** Schematic illustration of the fabrication of the NiTe-HfTe$_2$/g-C$_3$N$_4$ catalyst.

Fig. 1. Morphology and microstructure characterization of NiTe–HfTe$_2$/g-C$_3$N$_4$. FESEM image of NiTe–HfTe$_2$/g-C$_3$N$_4$ (a); TEM image of NiTe–HfTe$_2$/g-C$_3$N$_4$ (b).
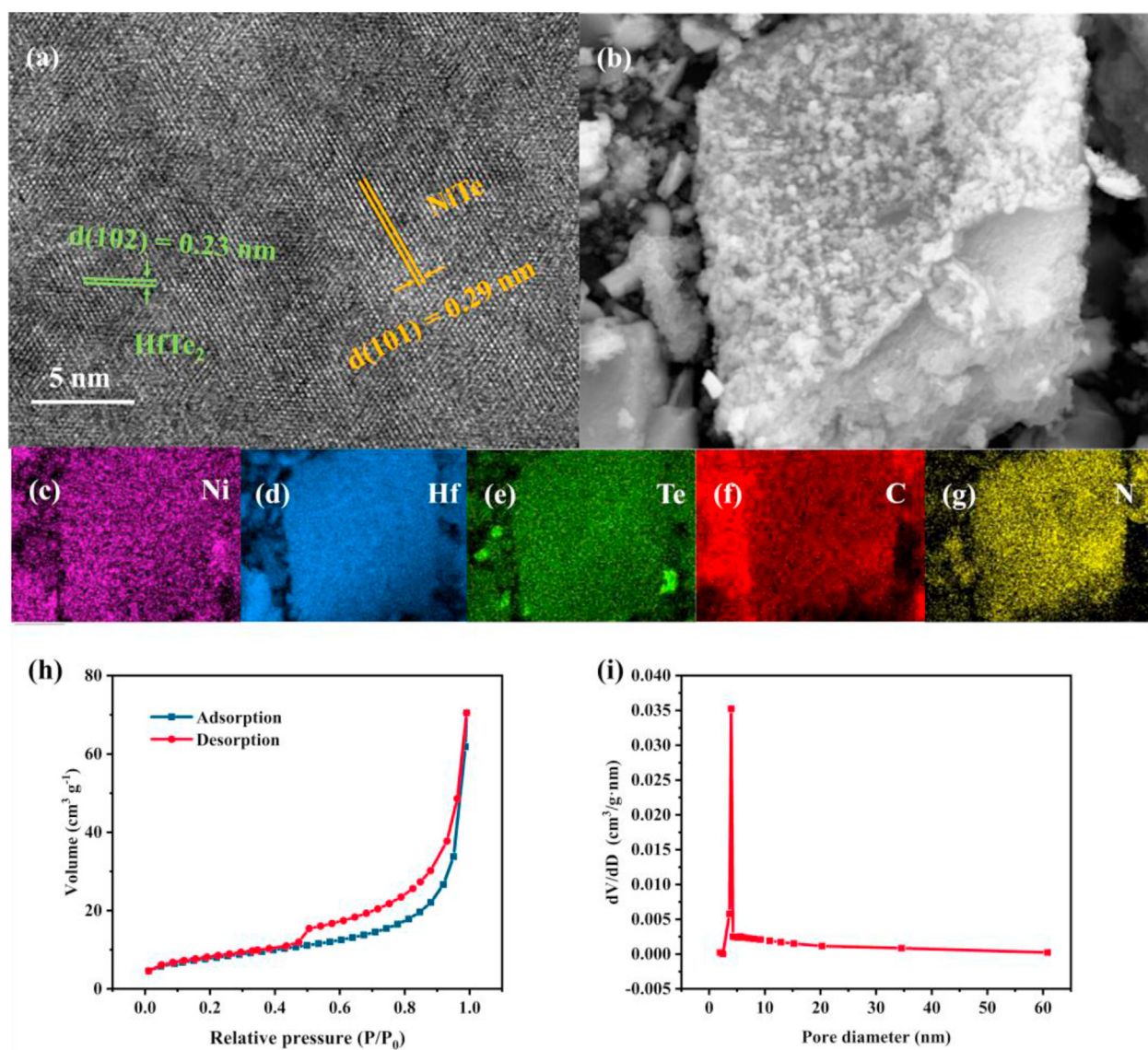
Fig. 2. Structural characterization of NiTe–HfTe$_2$/g-C$_3$N$_4$. HRTEM (a) image of NiTe–HfTe$_2$/g-C$_3$N$_4$; the selected area of NiTe–HfTe$_2$/g-C$_3$N$_4$ material (b) and corresponding elemental mapping images of Ni (c), Hf (d), Te (e), C (f), and N (g) elements; N$_2$ adsorption−desorption isotherm (h) and the Barrett-Joyner-Halenda (BJH) pore size distribution diagrams (i) of NiTe–HfTe$_2$/g-C$_3$N$_4$.
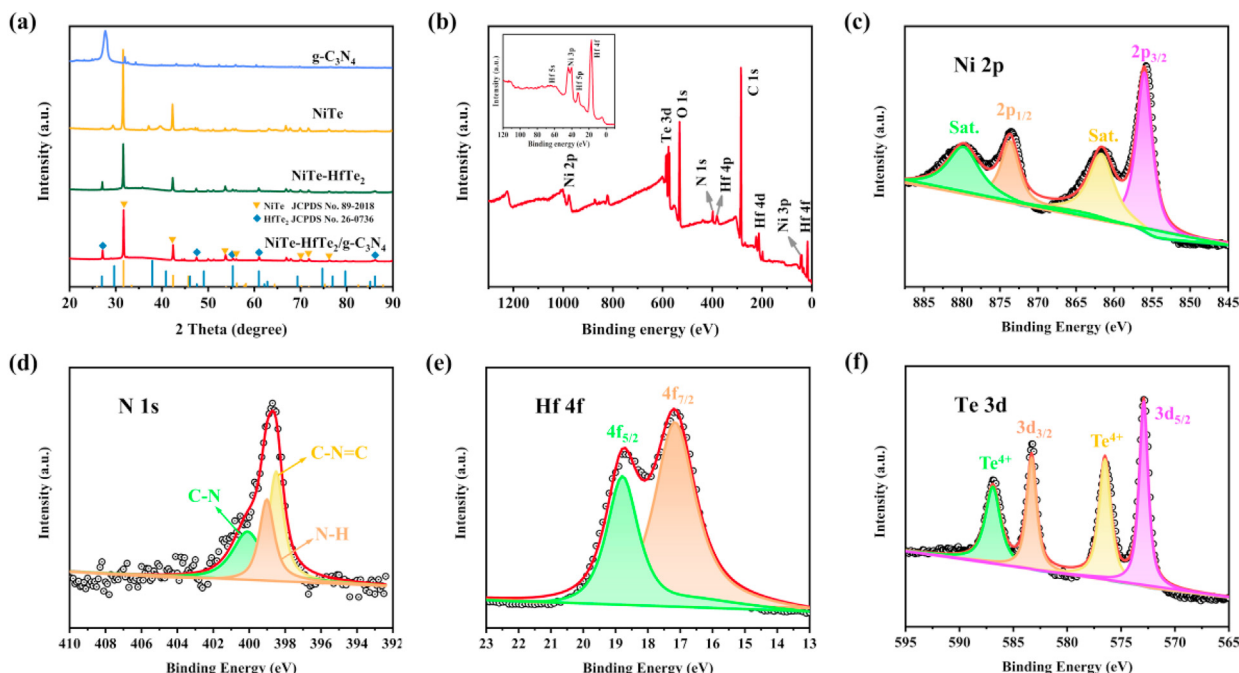
Fig. 3. Crystal and chemical composition analysis. XRD patterns of NiTe-HfTe$_2$/g-C$_3$N$_4$, NiTe-HfTe$_2$, NiTe, and g-C$_3$N$_4$ samples (a); XPS spectra of NiTe-HfTe$_2$/g-C$_3$N$_4$ (b); High-resolution XPS spectra of Ni 2p (c); N 1s (d); Hf 4f (e) and Te 3d (f) for as-prepared NiTe-HfTe$_2$/g-C$_3$N$_4$.

in detail via XPS analysis. As shown in Fig. 3b, we could clearly clarify the coexistence of Ni 2p (977 eV), Te 3d (576.1 eV), N 1s (298.1 eV), Hf 4p (282 eV), C 1s (285.2 eV), Hf 4d (213.2 eV), Hf 5s (69.5 eV), Ni 3p (42.3 eV), Hf 5p (33.5 eV), and Hf 4f (17.1 eV) orbitals in the XPS survey spectra of NiTe-HfTe$_2$/g-C$_3$N$_4$, showing the perfect coupling of NiTe and HfTe$_2$. The presence of O 1s (532.2 eV) orbital in the NiTe-HfTe$_2$/g-C$_3$N$_4$ may be attributed to oxidation because of air contact. In Fig. 3c−f, characteristic peaks and binding energies of Ni 2p, N 1s, Hf 4f, and Te 3d for NiTe-HfTe$_2$/g-C$_3$N$_4$ have been studied from high-resolution XPS spectra, respectively. In Fig. 3c, two main signals of Ni 2p are located at ~873.7 and ~856 eV belong to Ni 2p$_{1/2}$ and Ni 2p$_{3/2}$, respectively, indicating the Ni^{2+} ions remain stable in the composite materials [42−44]. Additionally, two other sub-peaks located at ~879.9 and ~861.7 eV, which are ascribed to the satellite peaks. From Fig. 3d, the high spectrum of N 1s can be divided into three main Gaussian-Lorenzian peaks. The peak centered at ~398.5 eV corresponds to the C-N = C (graphitic nitrogen). The spectrum existed at ~399 eV belongs to N−H (amino function). The signal located at ~400.1 eV related to C−N (pyridinic nitrogen) [45]. In Fig. 3e, Hf 4f level could be divided into two sublevels, Hf 4f$_{7/2}$ (17.2 eV) and Hf 4f$_{5/2}$ (18.8 eV). The Hf 4f$_{7/2}$ spectrum located at ~17.2 eV binding energy assigns to a high oxidation state Hf^{4+}, which may validate the successful synthesis of HfTe$_2$ [46]. As for Te 3d (Fig. 3f), the signals at ~583.3 and ~572.9 eV relate to Te^{2-} 3d$^{3/2}$ and Te^{2-} 3d$^{5/2}$ of NiTe and HfTe$_2$ in NiTe-HfTe$_2$/g-C$_3$N$_4$. This phenomenon directly proves the successful coupling of NiTe and HfTe$_2$. Furthermore, both two unmissable characteristic peaks at ~586.9 and ~576.5 eV are attributed to Te^{4+} because of the oxidation of Te during hydrothermal synthesis or upon air exposure [47,48]. Hence, all the previously mentioned results demonstrate the successful coupling of NiTe-HfTe$_2$/g-C$_3$N$_4$ bimetallic tellurides composites at the level of chemical functional groups and chemical bonds. However, the electrochemical performance of the as-prepared four samples needs to be further investigated; hence, additional electrochemical tests have been applied.

3.3. Electrochemical performance

Generally, electrocatalysts with ultralow overpotential, higher current density, and lower resistance value are considered as the promising electrocatalyst for applications widely. The electrochemical activities of as-prepared four samples for HER and OER were investigated using a typical three-electrode system in alkaline medium (0.1 M KOH) at room temperature with ~0.2 mg/cm^2 ink density. First, the OER performance of the NiTe-HfTe$_2$/g-C$_3$N$_4$ was assessed in alkaline electrolyte. At the same time, NiTe-HfTe$_2$, NiTe, g-C$_3$N$_4$, and commercial RuO$_2$ were also tested at the same condition. From the polarization curves of the five samples on OER tests in 0.1 M KOH (Fig. 4a), the results suggest that NiTe-HfTe$_2$/g-C$_3$N$_4$ possesses a substantial catalytic advantage over other samples, especially commercial OER electrocatalyst RuO$_2$. Fig. 4b summarizes the overpotential achieved by the NiTe-HfTe$_2$/g-C$_3$N$_4$ and other comparison samples at current densities (j) of 10, 50, and 100 mA/cm^2, respectively. Although the commercial electrocatalyst RuO$_2$ exhibits outstanding OER electrocatalytic activity, NiTe-HfTe$_2$/g-C$_3$N$_4$ reaches to current densities of 10, 50, and 100 mA/cm^2 only with the overpotential of 150, 220, and 260 mV, respectively. In addition, the as-prepared NiTe-HfTe$_2$/g-C$_3$N$_4$ electrocatalyst shows lower Tafel slope (47 mV/dec) than other samples in low overpotential region (Fig. 4c). Furthermore, exchange current density (J_0) is another important indicator in the evaluation of OER, which is influenced by electrode material, electrode surface state, electrolyte composition, and experimental temperature. The results show that NiTe-HfTe$_2$/g-C$_3$N$_4$ has the largest J_0 value (5.35 mA/cm^2), higher than that of NiTe-HfTe$_2$ (0.53 mA/cm^2), NiTe (0.44 mA/cm^2), and g-C$_3$N$_4$ (0.14 mA/cm^2), and even superior than RuO$_2$ (0.82 mA/cm^2). These results further suggest that NiTe-HfTe$_2$/g-C$_3$N$_4$ has better OER catalytic activity. Furthermore, the as-prepared advanced electrocatalyst displays outstanding oxygen evolution reaction electrocatalytic activity in alkaline and weak alkaline media (Fig. S3a). In a word, the new NiTe-HfTe$_2$/g-C$_3$N$_4$
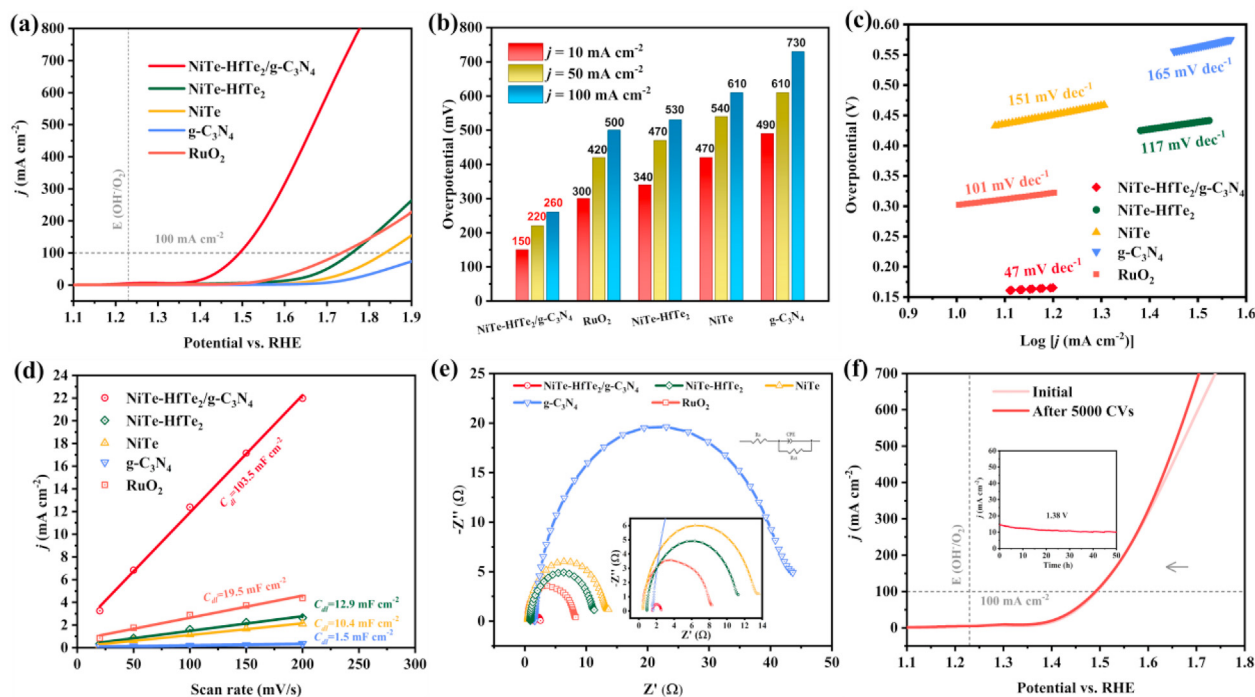
Fig. 4. Electrocatalytic OER performances of the catalysts in 0.1 M KOH electrolyte. Polarization curves (a) of as-prepared electrodes. Comparison of overpotentials (b) for various catalysts at current densities of 10, 50, and 100 mA/cm², respectively, and (c) the Tafel plots. (d) Estimation of C_{dl} by plotting the current density variation ($\Delta j = (j_a - j_c)/2$). (e) EIS Nyquist plots. (f) LSV curves of NiTe-HfTe₂/g-C₃N₄ electrode before and after 5,000 CV cycles. The inset image is the long-term durability test. All measurements were performed in O₂ purged 0.1 M KOH (pH ~13). All LSV curves were recorded at a sweep rate of 5 mV/s with iR corrected.

electrocatalyst synthesized by one-step simple solvothermal method exhibits satisfactory electrocatalytic performance.

Although the excellent performance of NiTe-HfTe₂/g-C₃N₄ advanced electrocatalyst has been demonstrated by polarization and Tafel curves, the mechanism for the efficient OER performance is not yet clear; therefore, additional electrochemically active surface areas were applied by scanning cyclic voltammetry. As displayed in Fig. 4d, the C_{dl} value of NiTe-HfTe₂/g-C₃N₄ electrode (103.5 mF/cm²) is larger than that of NiTe-HfTe₂ (12.9 mF/cm²), NiTe (10.4 mF/cm²), g-C₃N₄ (1.5 mF/cm²), and RuO₂ (19.5 mF/cm²), demonstrating the as-prepared NiTe-HfTe₂/g-C₃N₄ electrocatalyst possesses the largest electrochemical surface area (ECSA). The value of ECSA for NiTe-HfTe₂/g-C₃N₄ is 2,587.5 cm⁻², larger than that of NiTe-HfTe₂ (322.5 cm⁻²), NiTe (260 cm⁻²), g-C₃N₄ (37.5 cm⁻²), and RuO₂ (487.5 cm⁻²), in line with C_{dl} results. The turnover frequency (TOF) is another important parameter for characterizing the performance of electrochemical catalysts. We have calculated the TOF values of the as-prepared samples using electrochemical method. Unsurprisingly, NiTe-HfTe₂/g-C₃N₄ electrode still shows the largest TOF value (0.81 s⁻¹ at 350 mV) compared with NiTe-HfTe₂ electrode (0.040 s⁻¹ at 350 mV), NiTe electrode (0.007 s⁻¹ at 350 mV), g-C₃N₄ electrode (0.002 s⁻¹ at 350 mV), and noble RuO₂ catalysts electrode (0.039 s⁻¹ at 350 mV). Generally speaking, lower resistance means better electrocatalytic performance. The obtained NiTe-HfTe₂/g-C₃N₄ electrode possesses the smallest charge transferring resistance (R_{ct}) (1.2 Ω) using the Nyquist plots analysis (Fig .4e), which is much smaller than that of NiTe-HfTe₂ electrode (12.1 Ω), NiTe electrode (14.7 Ω), g-C₃N₄ electrode (45.1 Ω), and noble RuO₂ electrode (7.8 Ω), matching well with the results of polarization curves. Without excellent electrochemical stability, electrocatalysts could not be rolled out on a large scale; therefore, electrochemical stability is one of the key reference indicators for evaluating electrochemical performance. We have carried out 5,000 cycles CV test for NiTe-HfTe₂/g-C₃N₄ electrode (Fig. 4f),

finding that the linear sweep voltammetry (LSV) curve is close to the initial one, with no significant increases in overpotential at $j = 10$, 50, and 10 mA/cm². Furthermore, long-term stability test for the as-prepared NiTe-HfTe₂/g-C₃N₄ electrode at 1.38 V ($j = 10$ mA/cm²) shows no visible decrease in current density during 50 h continuous high-intensity testing, and the final current density still remains at 9.9 mA/cm². All the previously mentioned results demonstrate the unparalleled stability of the as-prepared NiTe-HfTe₂/g-C₃N₄, being attributed to the ultrathin layered g-C₃N₄ as stable substrates.

As for overall water splitting, the hydrogen evolution reaction is the important half-reaction; hence, efficient HER electrocatalytic performance of materials is essential for the development of advanced bifunctional electrocatalysts. As displayed in Fig. 5a, the current densities of as-prepared catalysts for HER were carried out by LSV method in the same alkaline media (0.1 M KOH). Although the electrocatalytic performance of NiTe-HfTe₂/g-C₃N₄ for HER is not as impressive as that of noble-metal-based Pt/C in the low voltage range, there is a huge improvement compared with NiTe-HfTe₂, NiTe, and g-C₃N₄. We have also summarized the overpotentials required to achieve different current densities ($j = 10$, 50, and 100 mA/cm²) for the as-prepared four samples and the commercial Pt/C, respectively (Fig. 5b). Obviously, the commercial HER electrocatalyst Pt/C exhibits unparalleled performance in the low voltage region, regardless of high or low current density, compared with other as-prepared samples. Surprisingly, NiTe-HfTe₂/g-C₃N₄ also displays satisfactory electrocatalytic capability, requiring only 71, 230, and 340 mV of overpotential to be overcome at current densities of 10, 50, and 100 mA/cm², respectively. Furthermore, NiTe-HfTe₂/g-C₃N₄ possesses the lowest Tafel slope (75 mV/dec) among the four as-prepared samples, close to the standard HER electrocatalyst Pt/C (41 mV/dec; Fig. 5c). Satisfactorily, the as-prepared NiTe-HfTe₂/g-C₃N₄ advanced bifunctional electrocatalyst possesses excellent HER electrocatalytic performance compared
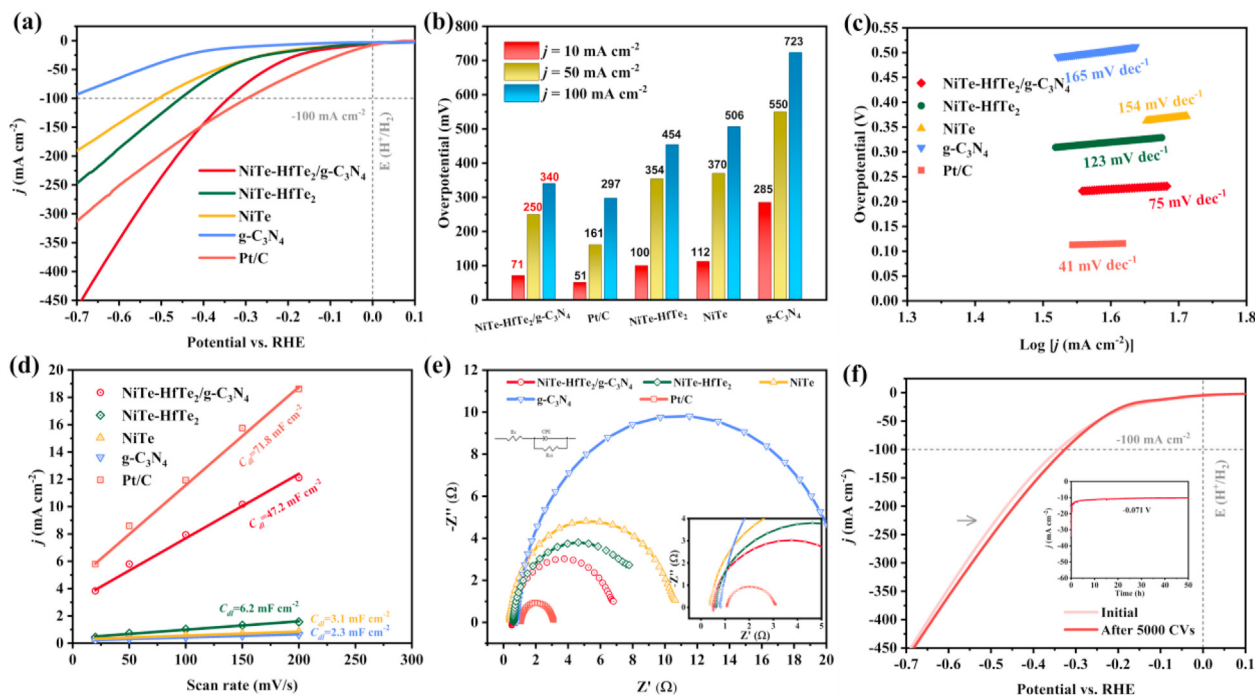
Fig. 5. Electrocatalytic HER performances of the catalysts in 0.1 M KOH electrolyte. Polarization curves (a) of as-prepared electrodes and their corresponding overpotentials (b) at 10, 50, and 100 mA/cm^2 and (c) corresponding Tafel plots. (d) Estimation of C_{dl} by plotting the current density variation ($\Delta j = (j_a - j_c)/2$). (e) EIS Nyquist plots. (f) Linear cyclic voltammetry curves of NiTe-HfTe$_2$/g-C$_3$N$_4$ electrode before and after 5,000 CV cycles. The inset image is the long-term HER durability test.
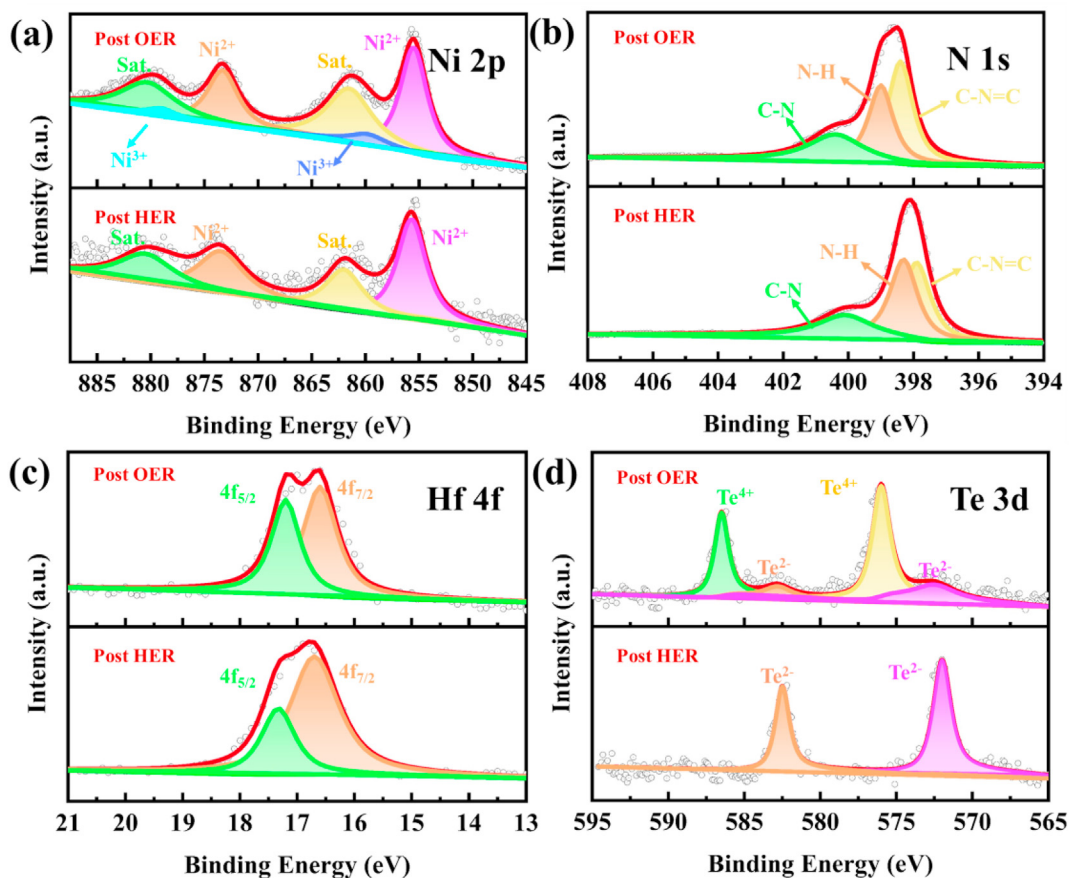

Fig. 6. XPS analysis after OER and HER chronoamperometric tests. (a–d) High-resolution XPS spectra of Ni 2p, N 1s, Hf 4f, and Te 3d for NiTe-HfTe$_2$/g-C$_3$N$_4$ after OER and HER stability test in 0.1 M KOH.

with the already developed overall water splitting samples (Table S4). We also carried out electrochemical active surface areas (Fig. 5d) and Nyquist plots (Fig. 5e) to directly probe the mechanism of the efficient HER catalytic activity of NiTe-HfTe$_2$/g-C$_3$N$_4$, and the results agreed well with the polarization curves. In addition, 5,000 cycles CV were applied to investigate the stability of NiTe-HfTe$_2$/g-C$_3$N$_4$ during the HER process (Fig. 5f), showing no significant increase in overpotential at low voltages and even a slight increase in the catalytic effect at high voltages. Moreover, the chronoamperometric test for as-obtained NiTe-HfTe$_2$/g-C$_3$N$_4$ catalyst at −0.071 V (j = 10 mA/cm^2) in 0.1 M KOH toward HER was conducted, indicating outstanding HER stability, and the sample maintained j = 10 mA/cm^2 after 50 h of continuous high voltage testing. All the previously mentioned results show that NiTe-HfTe$_2$/g-C$_3$N$_4$ does have almost perfect HER stability. In short, the high-effective electrocatalytic effect of NiTe-HfTe$_2$/g-C$_3$N$_4$ could be concluded as following: (1) the presence of Hf atoms enlarge the negative charge states on Te, shorting the lengths of Ni-Te bonds, lower reaction energy barriers; (2) strong synergistic effect of the early transition metal Hf and later transition metal Ni; (3) ultrathin g-C$_3$N$_4$ with large specific surface area, providing enough active sites for OH$^-$ adsorption.

Although electrochemical tests have been applied toward both OER and HER in 0.1 M KOH solution to discover the excellent stability of the NiTe-HfTe$_2$/g-C$_3$N$_4$, important information on microstructure, chemical bondings, and functional groups is not yet known. Therefore, additional SEM, HRTEM, and XPS analyses were used after OER and HER i-t tests conducted at 1.38 V (vs. RHE) and −0.071 V (vs. RHE) in 0.1 M KOH, respectively. It is worth

pointing out that the microscopic morphology of the NiTe-HfTe$_2$/g-C$_3$N$_4$ samples does not change too much after long-term testing (OER and HER) from SEM images (Fig. S11). The presence of Ni^{3+} in the image of HRTEM (Fig. S12) of NiTe-HfTe$_2$/g-C$_3$N$_4$ after the OER reaction is evidenced by the conspicuous NiOOH lattice fringe. Furthermore, the Ni 2p spectrum (Fig. 6a) exhibits Ni^{3+} signal peaks after long-term testing of the OER, attributed to the oxidation of Ni^{2+} during the OER process. As previously reported, NiOOH has significant facilitation effect on the OER process, which may explain the excellent OER catalytic performance of NiTe-HfTe$_2$/g-C$_3$N$_4$. As shown i.n Fig. 6b and c, the high-resolution XPS spectra of N 1s and Hf 4f do not change significantly after the OER and HER chronoamperometric tests, implying N and Hf elements are stably present in the NiTe-HfTe$_2$/g-C$_3$N$_4$ composition. In particular, the image of Te 3d is interesting in that the Te^{2-} signals weaken after long OER stability test (Fig. 6d), attributing to the oxidation of the low valent Te during anodic electrocatalysis; however, after long HER stability test, the characteristic peaks of Te^{4+} disappear, and only the regions corresponding to Te^{2-} remain, the phenomenon that could be explained by the reduction of the high valent Te during electrocatalysis at the cathode. Consequently, the obtained NiTe-HfTe$_2$/g-C$_3$N$_4$ electrocatalyst demonstrates superior chemical bondings and electrochemical performance stability toward both OER and HER in the alkaline media.

Benefited from the exceptional bifunctional property for OER and HER of NiTe-HfTe$_2$/g-C$_3$N$_4$, a simple two-electrode laboratory alkaline (0.1 M KOH) electrolyzer system, whose anode and cathode are both NiTe-HfTe$_2$/g-C$_3$N$_4$, was assembled to study overall water splitting. As displayed in Fig. 7a, the NiTe-HfTe$_2$/g-C$_3$N$_4$ electrode
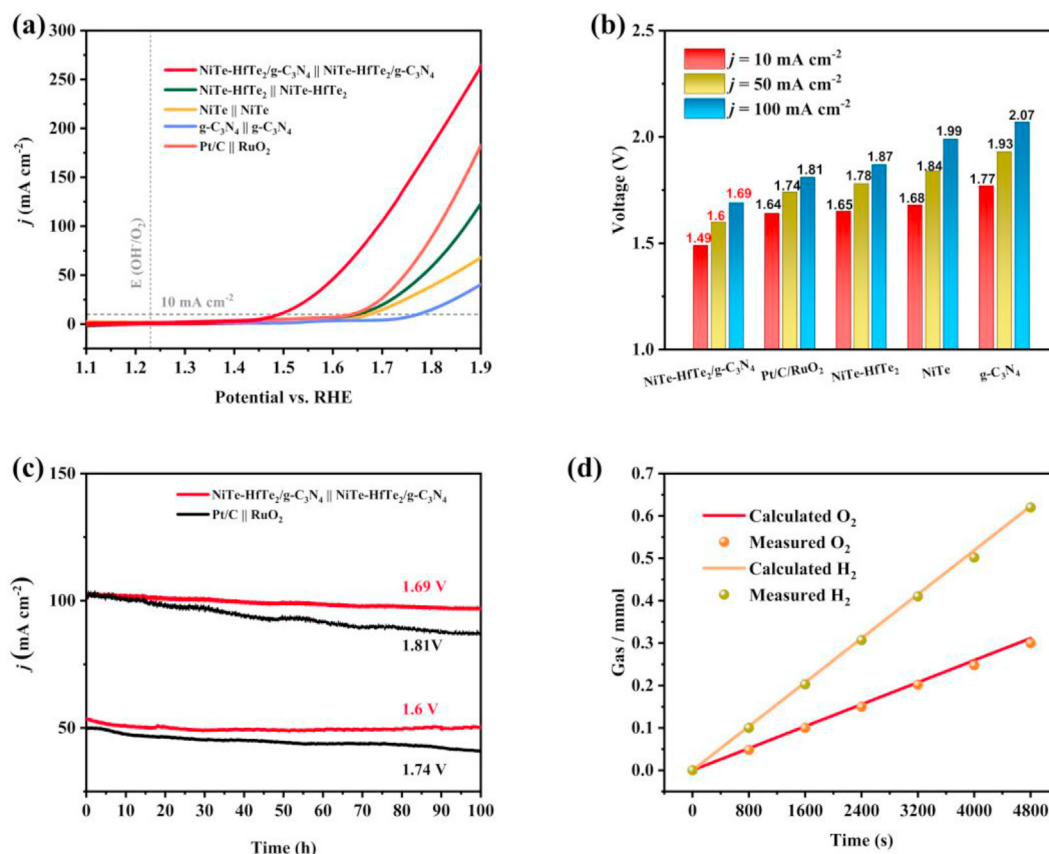

Fig. 7. Electrocatalytic overall water splitting performances of the catalysts in 0.1 M KOH electrolyte. (a) LSV curves of obtained samples in 0.1 M KOH, (b) and their corresponding cell voltages at j = 10, 50, and 100 mA/cm^2. (c) i-t curves of NiTe-HfTe$_2$/g-C$_3$N$_4$ || NiTe-HfTe$_2$/g-C$_3$N$_4$ and Pt/C || RuO$_2$ for 100 h at different operating voltages. (d) The measured and calculated amounts of O$_2$ and H$_2$ gases versus time measured at a constant current density of 100 mA cm^{-2}.

affords far surpassing activity than that of NiTe-HfTe$_2$, NiTe, g-C$_3$N$_4$, and precious-metal-based electrode Pt/C‖RuO$_2$. The electrolyzer combined by NiTe-HfTe$_2$/g-C$_3$N$_4$ provides current densities of 10, 50, and 100 mA/cm^2 in the cell voltage of 1.49, 1.6, and 1.69 V, respectively (Fig. 7b), which are lower than that of the electrolyzer assembled with commercial noble-based Pt/C‖RuO$_2$ (current densities of 10, 50, and 100 mA/cm^2 in the cell voltage of 1.64, 1.74, and 1.81 V, respectively). At the same time, the electrocatalytic activity of the electrolyzer combined by NiTe-HfTe$_2$/g-C$_3$N$_4$ is better than that of the electrolyzer based on NiTe-HfTe$_2$, NiTe, and g-C$_3$N$_4$. It is worth noting that the NiTe-HfTe$_2$/g-C$_3$N$_4$‖NiTe-HfTe$_2$/g-C$_3$N$_4$ showed impressive stability toward the full water splitting in long-term continuous voltage test as well. The current density (50 and 100 mA/cm^2) under different working voltages (1.6 and 1.69 V) remained close to 100% of the initial value after 100 h of high-intensity continuous full water splitting reaction (Fig. 7c). In contrast, the current of the electrolytic cell based on noble-metal-based Pt/C‖RuO$_2$ showed significant drops after long-term operation. These results further confirm the excellent stability of the as-prepared NiTe-HfTe$_2$/g-C$_3$N$_4$ electrode. Furthermore, the Faraday efficiency of H$_2$ and O$_2$ evolution were carried out by measuring the gases volumes. The measurement results showed that the collected molar ratio of H$_2$ and O$_2$ is close to 2:1 (theoretical value of the molar ratio of gas produced at the cathode and anode for overall water splitting), and the Faraday efficiency is 99% (Fig. 7d). In a word, the advanced bifunctional electrocatalysts prepared by one-step simple solvothermal method own outstanding electrocatalytic activity and satisfactory electrochemical stability, having promising potential in many commercial applications, such as clean energy conversation, eco-friendly fuel preparation, and so on.

4. Conclusions

In summary, we have successfully coupled an advanced electrocatalyst by simple one-step solvothermal method. Because of the large specific surface area of ultrathin g-C$_3$N$_4$ as substrates, NiTe-HfTe$_2$/g-C$_3$N$_4$ has abundant reactive sites and extremely low electron transfer resistance. For OER, the as-prepared sample possesses extremely low overpotentials of 150, 220, and 260 mV to reach to the current densities of 10, 50, and 100 mA/cm^2, respectively. For HER, the NiTe-HfTe$_2$/g-C$_3$N$_4$ also exhibits outstanding electrocatalytic properties, with impressively low overpotential of 71, 250, and 340 mV to drive current densities to 10, 50, and 100 mA/cm^2, respectively. As expected, the electrolytic cell with two electrodes assembled by NiTe-HfTe$_2$/g-C$_3$N$_4$ demonstrates the same excellent performance in full water splitting. In addition, NiTe-HfTe$_2$/g-C$_3$N$_4$ electrodes also exhibit much better electrochemical long-term stability than that of the commercial electrodes. This work may create a convenient route for the design and synthesis of novel transition metal−based electrocatalysts for overall water splitting.

Authors' contributions

T.L. contributed to formal analysis; writing, reviewing, and editing the article; validation; and investigation; J..W. contributed to conceptualization, methodology, software, supervision, funding acquisition, project administration. L.Q., Z.F., J.L., and B.W. contributed to resources, data curation, and software. Q.Z. contributed to project administration and supervision. J.C. contributed to resources, data curation, validation, visualization, and review of the article. L.P. contributed to resources and data curation. Z.C. contributed to resources, data curation, and validation.

Declaration of competing interest

The authors declare that they have no known competing financial interests or personal relationships that could have appeared to influence the work reported in this paper.

Acknowledgments

Appendix A. Supplementary data

Supplementary data to this article can be found online at https://doi.org/10.1016/j.mtener.2022.101002.

References

[1] L. Hao, M. Zhou, Y. Song, X. Ma, J. Wu, Q. Zhu, Z. Fu, Y. Liu, G. Hou, T. Li, Tin-based perovskite solar cells: further improve the performance of the electron transport layer-free structure by device simulation, Sol. Energy 230 (2021) 345−354, https://doi.org/10.1016/j.solener.2021.09.091.

[2] Z. Wang, J. Huang, L. Wang, Y. Liu, W. Liu, S. Zhao, Z.Q. Liu, Cation-tuning induced d-band center modulation on Co-based spinel oxide for oxygen reduction/evolution reaction, Angew Chem. Int. Ed. Engl. (2021), e202114696, https://doi.org/10.1002/anie.202114696.

[3] T. Li, X. Ma, J. Wu, F. Chu, L. Qiao, Y. Song, M. Wu, J. Lin, L. Peng, Z. Chen, Ni(OH)$_2$ microspheres in situ self-grown on ultra-thin layered g-C$_3$N$_4$ as a heterojunction electrocatalyst for oxygen evolution reaction, Electrochim. Acta 400 (2021) 139473, https://doi.org/10.1016/j.electacta.2021.139473.

[4] H. Wang, L. You, Y. Guan, H. Wang, X. Ma, D. Wang, J. Wu, Y. Zhu, J. Lin, J. Liu, Rational fabrication of flower-like VS$_2$-decorated Ti$_3$C$_2$ MXene heterojunction nanocomposites for supercapacitance performances, Colloids Surf. A 629 (2021) 127381, https://doi.org/10.1016/j.colsurfa.2021.127381.

[5] S. Zhao, C. Tan, C.-T. He, P. An, F. Xie, S. Jiang, Y. Zhu, K.-H. Wu, B. Zhang, H. Li, J. Zhang, Y. Chen, S. Liu, J. Dong, Z. Tang, Structural transformation of highly active metal−organic framework electrocatalysts during the oxygen evolution reaction, Nat. Energy 5 (11) (2020) 881−890, https://doi.org/10.1038/s41560-020-00709-1.

[6] X. Chen, C. Wang, Y. Liu, Y. Shen, Q. Zheng, S. Yang, H. Lu, H. Zou, K. Lin, H. Liu, H. Qiu, J. Wu, Q. Zhang, X. Liu, Popcorn-like aluminum-based powders for instant low-temperature water vapor hydrogen generation, Mater. Today Energy 19 (2021), https://doi.org/10.1016/j.mtener.2020.100602.

[7] T.L.L. Doan, D.C. Nguyen, S. Prabhakaran, D.H. Kim, D.T. Tran, N.H. Kim, J.H. Lee, Single-atom Co-decorated MoS$_2$ nanosheets assembled on metal nitride nanorod arrays as an efficient bifunctional electrocatalyst for pH-universal water splitting, Adv. Funct. Mater. 31 (2021) 2100233, https://doi.org/10.1002/adfm.202100233.

[8] X. Cheng, Y. Lu, L. Zheng, M. Pupucevski, H. Li, G. Chen, S. Sun, G. Wu, Engineering local coordination environment of atomically dispersed platinum catalyst via lattice distortion of support for efficient hydrogen evolution reaction, Mater. Today Energy 20 (2021), https://doi.org/10.1016/j.mtener.2021.100653.

[9] Y. Liu, H.T.D. Bui, A.R. Jadhav, T. Yang, S. Saqlain, Y. Luo, J. Yu, A. Kumar, H. Wang, L. Wang, V.Q. Bui, M.G. Kim, Y.D. Kim, H. Lee, Revealing the synergy of cation and anion vacancies on improving overall water splitting kinetics, Adv. Funct. Mater. 31 (2021) 2010718, https://doi.org/10.1002/adfm.202010718.

[10] Z. Zhou, Y. Kong, H. Tan, Q. Huang, C. Wang, Z. Pei, H. Wang, Y. Liu, Y. Wang, S. Li, X. Liao, W. Yan, S. Zhao, Cation-vacancy-enriched nickel phosphide for efficient electrosynthesis of hydrogen peroxides, Adv. Mater. (2022), e2106541, https://doi.org/10.1002/adma.202106541.

[11] J. Gao, Y. Zhang, X. Wang, L. Jia, H. Jiang, M. Huang, A. Toghan, Nitrogen-doped Sr$_2$Fe$_{1.5}$Mo$_{0.5}$O$_{6-\delta}$ perovskite as an efficient and stable catalyst for hydrogen evolution reaction, Mater. Today Energy 20 (2021), https://doi.org/10.1016/j.mtener.2021.100695.

[12] S. Zhao, Y. Yang, Z. Tang, Insight into structural evolution, active sites, and stability of heterogeneous electrocatalysts, Angew Chem. Int. Ed. Engl. 61 (11) (2022), e202110186, https://doi.org/10.1002/anie.202110186.

[13] M. Kuang, P. Han, Q. Wang, J. Li, G. Zheng, CuCo hybrid oxides as bifunctional electrocatalyst for efficient water splitting, Adv. Funct. Mater. 26 (2016) 8555−8561, https://doi.org/10.1002/adfm.201604804.

[14] D. Liang, H. Zhang, X. Ma, S. Liu, J. Mao, H. Fang, J. Yu, Z. Guo, T. Huang, MOFs-derived core-shell Co$_3$Fe$_7$@Fe$_2$N nanopaticles supported on r-GO as high-

performance bifunctional electrocatalyst for oxygen reduction and oxygen evolution reactions, Mater, Today Energy 17 (2020), https://doi.org/10.1016/j.mtener.2020.100433.

[15] J. Ren, M. Antonietti, T.-P. Fellinger, Efficient water splitting using a simple Ni/N/C paper electrocatalyst, Adv. Energy Mater. 5 (2015) 1401660, https://doi.org/10.1002/aenm.201401660.

[16] J. Ge, D. Zhang, J. Jin, X. Han, Y. Wang, F. Zhang, X. Lei, Oxygen atoms substituting sulfur atoms of MoS₂ to activate the basal plane and induce the phase transition for boosting hydrogen evolution, Mater, Today Energy 22 (2021), https://doi.org/10.1016/j.mtener.2021.100854.

[17] B. Ren, D. Li, Q. Jin, H. Cui, C. Wang, In-situ tailoring cobalt nickel molybdenum oxide components for overall water-splitting at high current densities, Chem-electrochem 6 (2019) 413−420, https://doi.org/10.1002/celc.201801386.

[18] H. Wang, H.W. Lee, Y. Deng, Z. Lu, P.C. Hsu, Y. Liu, D. Lin, Y. Cui, Bifunctional non-noble metal oxide nanoparticle electrocatalysts through lithium-induced conversion for overall water splitting, Nat. Commun. 6 (2015) 7261, https://doi.org/10.1038/ncomms8261.

[19] J.H. Qin, W.J. Qin, Z. Xiao, J.K. Yang, H.R. Wang, X.G. Yang, D.S. Li, L.F. Ma, Efficient energy-transfer-induced high photoelectric conversion in a dye-encapsulated ionic pyrene-based metal-organic framework, Inorg. Chem. 60 (24) (2021) 18593−18597, https://doi.org/10.1021/acs.inorgchem.1c02624.

[20] B. Zhang, C. Xiao, S. Xie, J. Liang, X. Chen, Y. Tang, Iron−Nickel nitride nano-structures in situ grown on surface-redox-etching nickel foam: efficient and ultrasustainable electrocatalysts for overall water splitting, Chem. Mater. 28 (2016) 6934−6941, https://doi.org/10.1021/acs.chemmater.6b02610.

[21] M. Ledendecker, S. Krick Calderon, C. Papp, H.P. Steinruck, M. Antonietti, M. Shalom, The synthesis of nanostructured Ni₅P₄ films and their use as a non-noble bifunctional electrocatalyst for full water splitting, Angew Chem. Int. Ed. Engl. 54 (2015) 12361−12365, https://doi.org/10.1002/anie.201502438.

[22] P.W. Menezes, A. Indra, C. Das, C. Walter, C. Göbel, V. Gutkin, D. Schmeiβer, M. Driess, Uncovering the nature of active species of nickel phosphide cata-lysts in high-performance electrochemical overall water splitting, ACS Catal. 7 (2016) 103−109, https://doi.org/10.1021/acscatal.6b02666.

[23] P. Luo, H. Zhang, L. Liu, Y. Zhang, J. Deng, C. Xu, N. Hu, Y. Wang, Targeted synthesis of unique nickel sulfide (NiS, NiS₂) microarchitectures and the ap-plications for the enhanced water splitting system, ACS Appl. Mater. Interfaces 9 (2017) 2500−2508, https://doi.org/10.1021/acsami.6b13984.

[24] W. Zhu, X. Yue, W. Zhang, S. Yu, Y. Zhang, J. Wang, J. Wang, Nickel sulfide microsphere film on Ni foam as an efficient bifunctional electrocatalyst for overall water splitting, Chem. Commun. 52 (2016) 1486−1489, https://doi.org/10.1039/c5cc08064a.

[25] B.H.R. Suryanto, Y. Wang, R.K. Hocking, W. Adamson, C. Zhao, Overall elec-trochemical splitting of water at the heterogeneous interface of nickel and iron oxide, Nat. Commun. 10 (2019) 5599, https://doi.org/10.1038/s41467-019-13415-8.

[26] X. Zou, Y. Wu, Y. Liu, D. Liu, W. Li, L. Gu, H. Liu, P. Wang, L. Sun, Y. Zhang, In situ generation of bifunctional, efficient Fe-based catalysts from mackinawite iron sulfide for water splitting, Inside Chem. 4 (2018) 1139−1152, https://doi.org/10.1016/j.chempr.2018.02.023.

[27] N. Jiang, B. You, M. Sheng, Y. Sun, Electrodeposited cobalt-phosphorous-derived films as competent bifunctional catalysts for overall water splitting, Angew Chem. Int. Ed. Engl. 54 (2015) 6251−6254, https://doi.org/10.1002/anie.201501616.

[28] J. Liu, C. Wang, H. Sun, H. Wang, F. Rong, L. He, Y. Lou, S. Zhang, Z. Zhang, M. Du, CoOₓ/CoNy nanoparticles encapsulated carbon-nitride nanosheets as an efficiently trifunctional electrocatalyst for overall water splitting and Zn-air battery, Appl. Catal. B Environ. 279 (2020) 119407, https://doi.org/10.1016/j.apcatb.2020.119407.

[29] A. Sivanantham, S. Shanmugam, Nickel selenide supported on nickel foam as an efficient and durable non-precious electrocatalyst for the alkaline water electrolysis, Appl. Catal. B Environ. 203 (2017) 485−493, https://doi.org/10.1016/j.apcatb.2016.10.050.

[30] P. Wang, Z. Pu, W. Li, J. Zhu, C. Zhang, Y. Zhao, S. Mu, Coupling NiSe₂-Ni₂P heterostructure nanowrinkles for highly efficient overall water splitting, J. Catal. 377 (2019) 600−608, https://doi.org/10.1016/j.jcat.2019.08.005.

[31] J. Liu, D. Zhu, T. Ling, A. Vasileff, S.-Z. Qiao, S-NiFe₂O₄ ultra-small nanoparticle built nanosheets for efficient water splitting in alkaline and neutral pH, Nano Energy 40 (2017) 264−273, https://doi.org/10.1016/j.nanoen.2017.08.031.

[32] Y. Zhu, W. Zhou, Y. Zhong, Y. Bu, X. Chen, Q. Zhong, M. Liu, Z. Shao, A perovskite nanorod as bifunctional electrocatalyst for overall water split-ting, Adv. Energy Mater. 7 (2017) 1602122, https://doi.org/10.1002/aenm.201602122.

[33] Y. Liu, Q. Li, R. Si, G.D. Li, W. Li, D.P. Liu, D. Wang, L. Sun, Y. Zhang, X. Zou, Coupling sub-nanometric copper clusters with quasi-amorphous cobalt sulfide yields efficient and robust electrocatalysts for water splitting reac-tion, Adv. Mater. 29 (2017) 1606200, https://doi.org/10.1002/adma.201606200.

[34] J. Wang, H.X. Zhong, Z.L. Wang, F.L. Meng, X.B. Zhang, Integrated three-dimensional carbon paper/carbon tubes/cobalt-sulfide sheets as an efficient electrode for overall water splitting, ACS Nano 10 (2016) 2342−2348, https://doi.org/10.1021/acsnano.5b07126.

[35] Y. Hou, M.R. Lohe, J. Zhang, S. Liu, X. Zhuang, X. Feng, Vertically oriented cobalt selenide/NiFe layered-double-hydroxide nanosheets supported on exfoliated graphene foil: an efficient 3D electrode for overall water split-ting, Energy Environ. Sci. 9 (2016) 478−483, https://doi.org/10.1039/c5ee03440j.

[36] J.H. Qin, H. Zhang, P. Sun, Y.D. Huang, Q. Shen, X.G. Yang, L.F. Ma, Ionic liquid induced highly dense assembly of porphyrin in MOF nanosheets for photo-dynamic therapy, Dalton Trans. 49 (48) (2020) 17772−17778, https://doi.org/10.1039/d0dt03031g.

[37] L. Tao, M. Huang, S. Guo, Q. Wang, M. Li, X. Xiao, G. Cao, Y. Shao, Y. Shen, Y. Fu, M. Wang, Surface modification of NiCo₂Te₄ nanoclusters: a highly effi-cient electrocatalyst for overall water-splitting in neutral solution, Appl. Catal. B Environ. 254 424-431. https://doi.org/10.1016/j.apcatb.2019.05.010.

[38] X. Wang, X. Huang, W. Gao, Y. Tang, P. Jiang, K. Lan, R. Yang, B. Wang, R. Li, Metal-organic framework derived CoTe₂ encapsulated in nitrogen-doped carbon nanotube frameworks: a high-efficiency bifunctional electrocatalyst for overall water splitting, J. Mater. Chem. 6 (2018) 3684−3691, https://doi.org/10.1039/c7ta10728e.

[39] R.J. Toh, Z. Sofer, M. Pumera, Catalytic properties of group 4 transition metal dichalcogenides (MX2; M = Ti, Zr, Hf; X = S, Se, Te), J. Mater. Chem. 4 (2016) 18322−18334, https://doi.org/10.1039/c6ta08089h.

[40] J.O.M. Bockris, T. Otagawa, The electrocatalysis of oxygen evolution on pe-rovskites, J. Electrochem. Soc. 131 (2019) 290−302, https://doi.org/10.1149/1.2115565.

[41] F. Zhao, B. Wen, W. Niu, Z. Chen, C. Yan, A. Selloni, C.G. Tully, X. Yang, B.E. Koel, Increasing iridium oxide activity for the oxygen evolution reaction with hafnium modification, J. Am. Chem. Soc. 143 (2021) 15616−15623, https://doi.org/10.1021/jacs.1c03473.

[42] M.K. Bates, Q. Jia, H. Doan, W. Liang, S. Mukerjee, Charge-transfer effects in Ni-Fe and Ni-Fe-Co mixed-metal oxides for the alkaline oxygen evolution reac-tion, ACS Catal. 6 (2015) 155−161, https://doi.org/10.1021/acscatal.5b01481.

[43] J. Du, Z. Zou, C. Liu, C. Xu, Hierarchical Fe-doped Ni₃Se₄ ultrathin nanosheets as an efficient electrocatalyst for oxygen evolution reaction, Nanoscale 10 (2018) 5163−5170, https://doi.org/10.1039/c8nr00426a.

[44] Z. Zhao, H. Wu, H. He, X. Xu, Y. Jin, A high-performance binary Ni-Co hy-droxide-based water oxidation electrode with three-dimensional coaxial nanotube Array structure, Adv. Funct. Mater. 24 (2014) 4698−4705, https://doi.org/10.1002/adfm.201400118.

[45] F. Wang, Y. Zhao, M. Zhang, J. Wu, G. Liu, P. He, Y. Qi, X. Li, Y. Zhou, J. Li, Bimetallic sulfides ZnIn₂S₄ modified g-C₃N₄ adsorbent with wide temperature range for rapid elemental mercury uptake from coal-fired flue gas, Chem. Eng. J. 426 (2021) 131343, https://doi.org/10.1016/j.cej.2021.131343.

[46] X. Yang, F. Zhao, Y.W. Yeh, R.S. Selinsky, Z. Chen, N. Yao, C.G. Tully, Y. Ju, B.E. Koel, Nitrogen-plasma treated hafnium oxyhydroxide as an efficient acid-stable electrocatalyst for hydrogen evolution and oxidation reactions, Nat. Commun. 10 (2019) 1543, https://doi.org/10.1038/s41467-019-09162-5.

[47] L. Hu, X. Zeng, X. Wei, H. Wang, Y. Wu, W. Gu, L. Shi, C. Zhu, Interface engi-neering for enhancing electrocatalytic oxygen evolution of NiFe LDH/NiTe heterostructures, Appl. Catal. B Environ. 273 (2020) 119014, https://doi.org/10.1016/j.apcatb.2020.119014.

[48] J. Xu, Y. Yin, H. Xiong, X. Du, Y. Jiang, W. Guo, Z. Wang, Z. Xie, D. Qu, H. Tang, Q. Deng, J. Li, Improving catalytic activity of metal telluride by hybridization: an efficient Ni₃Te₂-CoTe composite electrocatalyst for oxygen evolution re-action, Appl. Surf. Sci. 490 (2019) 516−521, https://doi.org/10.1016/j.apsusc.2019.06.080.
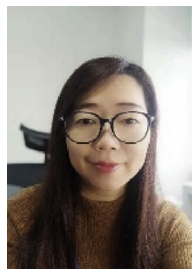
Tong Li, Graduate student in College of Energy and Mechanical Engineering at the Shanghai University of Electric power. His research interests are mainly focused on green energy and overall water splitting.

Jia Lin, Ph. D, Professor in College of Mathematics and Physics at the Shanghai University of Electric power. His research interests are mainly focused on optics, photonics, optoelectronics and energy materials.

Jiang Wu, Ph. D, Professor in College of Energy and Mechanical Engineering at the Shanghai University of Electric power. His research interests are mainly focused on photocatalysis and eletrocatalysis, as well as in the field of combustion and pollutant control.

Jing Chen, Ph. D, Professor in College of Mathematics and Physics at the Shanghai University of Electric power. Her research interests are mainly focused on semiconductor physics and device, spectroscopic study of novel semiconductor materials.

Lingxia Qiao, Graduate student in College of Energy and Mechanical Engineering at the Shanghai University of Electric power. Her research interests are focused on oxygen evolution reaction and electrocatalysis.

Lin Peng, Ph. D, Professor in College of Mathematics and Physics at the Shanghai University of Electric power. His research interests are mainly focused on new energy materials and devices.

Qunzhi Zhu, Ph. D, Professor in College of Energy and Mechanical Engineering at the Shanghai University of Electric power. His research interests are mainly focused on solar thermal utilization, distributed energy systems and industrial energy-saving technologies.

Baofeng Wang, Ph. D, Professor in College of Environmental and Chemical Engineering at the Shanghai University of Electric power. His research interests are mainly focused on the key materials (cathode and anode materials, electrolytes, binders) for new chemical power sources.

Zaiguo Fu, Ph. D, Professor in College of Energy and Mechanical Engineering at the Shanghai University of Electric power. His research interests are mainly focused on turbulent and reduced resistance flow in engineering thermophysics.

Zhongwei Chen, Ph. D, Professor in Advanced Materials for Clean Energy at the University of Waterloo. His research interests are in the development of advanced electrochemical energy materials and systems for fuel cells and batteries.